



PAPER

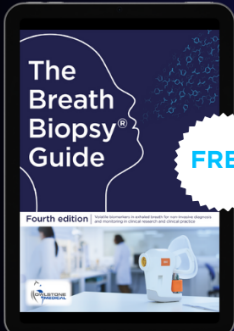
Characterization of silicon carbide and diamond detectors for neutron applications

To cite this article: M Hodgson *et al* 2017 *Meas. Sci. Technol.* **28** 105501

View the [article online](#) for updates and enhancements.

You may also like

- [Multi-spectral pyrometry—a review](#)
António Araújo
- [Interfacial properties of hydrides in -Zr: a theoretical study](#)
M-A Louchez, R Besson, L Thuinet et al.
- [Development of a commercially viable piezoelectric force sensor system for static force measurement](#)
Jun Liu, Xinwei Luo, Jingcheng Liu et al.



FREE **The Breath Biopsy® Guide**
Fourth edition

[DOWNLOAD THE FREE E-BOOK](#)

BREATH BIOPSY®



Characterization of silicon carbide and diamond detectors for neutron applications

M Hodgson¹ , A Lohstroh¹, P Sellin¹ and D Thomas²

¹ Department of Physics, University of Surrey, Guildford, GU2 7XH, United Kingdom

² 2NPL, Teddington, TW11 0LW, United Kingdom

E-mail: michael.hodgson@becq.co.uk

Received 14 January 2017, revised 5 March 2017

Accepted for publication 13 July 2017

Published 12 September 2017



Abstract

The presence of carbon atoms in silicon carbide and diamond makes these materials ideal candidates for direct fast neutron detectors. Furthermore the low atomic number, strong covalent bonds, high displacement energies, wide bandgap and low intrinsic carrier concentrations make these semiconductor detectors potentially suitable for applications where rugged, high-temperature, low-gamma-sensitivity detectors are required, such as active interrogation, electronic personal neutron dosimetry and harsh environment detectors.

A thorough direct performance comparison of the detection capabilities of semi-insulating silicon carbide (SiC–SI), single crystal diamond (D–SC), polycrystalline diamond (D–PC) and a self-biased epitaxial silicon carbide (SiC–EP) detector has been conducted and benchmarked against a commercial silicon PIN (Si–PIN) diode, in a wide range of alpha (Am-241), beta (Sr/Y-90), ionizing photon (65 keV to 1332 keV) and neutron radiation fields (including 1.2 MeV to 16.5 MeV mono-energetic neutrons, as well as neutrons from AmBe and Cf-252 sources).

All detectors were shown to be able to directly detect and distinguish both the different radiation types and energies by using a simple energy threshold discrimination method. The SiC devices demonstrated the best neutron energy discrimination ratio ($E_{\max}(n = 5 \text{ MeV})/E_{\max}(n = 1 \text{ MeV}) \approx 5$), whereas a superior neutron/photon cross-sensitivity ratio was observed in the D–PC detector ($E_{\max}(\text{AmBe})/E_{\max}(\text{Co-60}) \approx 16$). Further work also demonstrated that the cross-sensitivity ratios can be improved through use of a simple proton-recoil conversion layer.

Stability issues were also observed in the D–SC, D–PC and SiC–SI detectors while under irradiation, namely a change of energy peak position and/or count rate with time (often referred to as the polarization effect). This phenomenon within the detectors was non-debilitating over the time period tested (>5 h) and, as such, stable operation was possible.

Furthermore, the D–SC, self-biased SiC–EP and semi-insulating SiC detectors were shown to operate over the temperature range $-60 \text{ }^{\circ}\text{C}$ to $+100 \text{ }^{\circ}\text{C}$.

Keywords: epitaxial silicon carbide, semi-insulating silicon carbide, single crystal diamond, polycrystalline diamond, neutron detectors, semiconductor radiation detectors, radiation hard semiconductor detectors

(Some figures may appear in colour only in the online journal)

1. Introduction

Silicon carbide (4H-SiC) and chemical vapour deposited diamond (CVD-D) semiconductors have been suggested as ideal devices for detecting neutrons in a number of specialist applications [1–4].

Despite a relatively small detection volume compared with other neutron detection devices, they present the ability to directly detect fast neutrons due to the carbon atoms present, removing issues associated with conversion layers [5]. The thin material and low atomic number (Z) also reduces

the sensitivity to ionizing photon radiation, which is essential as neutron fields are typically accompanied by x-rays and/or gamma-rays.

The high threshold displacement energy of the material leads to a high level of radiation hardness compared with other common semiconductor detector materials [6, 7], whereas the strong covalent bonds between atoms also make the materials mechanically strong.

Furthermore, the wide bandgap and low intrinsic carrier concentration of these materials lead to low leakage current densities over a wide range of temperatures [6, 8], allowing for stable operation in practical non-laboratory systems. This, coupled with low capacitance values for bulk undoped materials, potentially makes these detectors suitable for scaling up to large-area devices without significant effects upon their capabilities.

In this work we present a complete and direct comparison of the main variants of 4H-SiC and CVD-D to assess their suitability for neutron detection applications. In particular the neutron and gamma intrinsic efficiency as a function of radiation energy has been determined and compared with a standard silicon PIN photodiode (Si-PIN) to give a practical performance benchmark against a commercial semiconductor. Epitaxial SiC (SiC-EP), bulk semi-insulating SiC (SiC-SI), electronic grade single-crystal D (D-SC) and polycrystalline D (D-PC) radiation detectors were all individually irradiated with alpha particles (Am-241), beta particles (Sr/Y-90), ionizing photons (0.065 MeV to 1.332 MeV, $3000 \gamma \text{ s}^{-1}$ to $1 \times 10^7 \gamma \text{ s}^{-1}$) and neutrons (1.2 MeV to 16.5 MeV, as well as AmBe and Cf-252, 250 n s^{-1} to 4500 n s^{-1}). The SiC-EP, SiC-SI and D-SC detectors were also irradiated with Am-241 alpha particles over a temperature range of $-60 \text{ }^\circ\text{C}$ to $+100 \text{ }^\circ\text{C}$.

2. Neutron applications

2.1. Active interrogation

Most active interrogation techniques utilize external radiation sources (usually neutrons and photons) to probe and identify the objects under investigation. In principle this technique has been used for many years in medical x-ray machines, baggage scanners and nuclear fuel cycle survey instruments [9]. However, since the mid-1990s there has also been significant interest in homeland security applications with the aim of preventing the illegal movement of nuclear material across ports and borders. This technique uses sources with high fluence and energy radiation, usually accelerator based, to induce fission within the nuclear materials and detect the signature products [10].

The detection system used in security-based active interrogation systems needs to be robust and capable of operating in relatively challenging radiological conditions. Regardless of the interrogation type, a mixed field of radiation will be present during operation from the initial interrogation pulse, fission reaction, material activation and scattering. Therefore any suitable detection system must be able to distinguish between

neutron- and photon-induced signals. Furthermore, in order to determine whether the characteristic neutron emissions are prompt fission neutrons (2–5 MeV) or delayed/scattered neutrons ($<2 \text{ MeV}$) [11], discrimination between different energies is also required [12].

The radiation sources are generally quick, high-intensity pulses [10] with the subsequent characteristic fissile radiations ranging between prompt nanosecond emissions and delayed emissions over seconds, minutes and even hours. As such, the detector system must be able to operate over a wide dynamic range, as well operate in, or rapidly recover from, the high-intensity interrogation pulse so that the induced emissions can be quickly detected ($\sim 1 \text{ ms}$ [12]).

In order for practical roll-out at ports and borders the detectors must be stable during operation ($>1 \text{ min}$) over a range of environmental conditions ($-30 \text{ }^\circ\text{C}$ to $+55 \text{ }^\circ\text{C}$ [12]). Furthermore, regular exposures of high-flux and high-energy radiation fields must not result in any radiation-induced damage over the operational life-time of the detection system (typically around 5 years as a minimum [12]).

2.2. Electronic personal neutron dosimetry

Electronic personal neutron dosimeters are part of an established international industry spanning nuclear power, medical, defence and emergency services. The dominant models on the market use multiple silicon photodiodes with various filters or convertor layers to detect beta, x-ray, gamma and/or neutron radiation [13–15].

For most devices, neutron detection in electronic dosimeters is achieved by using Si detectors with several neutron conversion layers [14, 15] to give a characteristic energy response, which for the most part is similar for the majority of devices on the market [16, 17]. However, maintaining a flat dose equivalent response over such a wide range of energies (0.025 eV to 15 MeV) is extremely difficult, with the neutron personal dose equivalent relative response of these devices often ranging from ≈ 0.1 to 15 [16].

One of the reasons for this non-uniformity is related to how the different detector channels are combined. Detection thresholds within these devices are set in order to minimize the cross-sensitivity to gamma radiation on the same channel. However, this threshold will also limit the detection of lower-energy conversion particles, affecting the overlap between the detector channels and subsequently how they are combined.

A further issue with these devices is that the fundamental sensitivity to neutrons (counts/dose) is usually quite poor, requiring relatively high doses before statistically significant readings can be considered. Although this is in some way a result of the inefficiencies related to conversion layers [5], it is more likely related to the relatively small size of the detectors limiting the probability of detection. Although larger-area detectors allow more particles to be detected, increasing the ability to detect fast neutrons, this is at the expense of higher leakage current, capacitance and an increase in gamma cross-sensitivity (i.e. more gamma-ray photons are detected).

Table 1. Main detectors under investigation. The values given in the format X : X correspond to the position relative to the detector material, in this case represented by ‘:’. Furthermore, in the ‘Contact material’ column (S) and (O) correspond to Schottky barrier contact and ohmic contact, respectively.

Detector	Material manufacturer	Material	Thickness (μm)	Contact material	Contact size (mm)	Contact thickness (nm)
Si-PIN	Hamamatsu [©]	Si	≈ 300	—	3.6×3.6	—
SiC-EP	Cree [©]	4H-SiC	$50 + 360$	(O) Au/Pt/Ti : Ni/Au (S)	$\varnothing 5$	150/30/20 : 100/100
SiC-SI	Cree [©]	4H-SiC	350	(O) Au/Ni : Ti/Pt/Au (S)	5×5	1500/40 : 60/40/2000
SiC-SI-Cr3	Cree [©]	4H-SiC	350	(O) Au/Ni : Ti/Pt/Au (S)	9×9	100/100 : 30/20/100
SiC-SI-Cr4	Cree [©]	4H-SiC	350	(O) Au/Ni : Ti/Pt/Au (S)	2×2	1500/40 : 30/20/100
SiC-SI-Cr5	Cree [©]	4H-SiC	350	(O) Au/Ni : Ti/Pt/Au (S)	5×5	1500/40 : 30/20/100
D-SC	Element six [©]	CVD-D	500	Pt : Pt	4×4	120 : 120
D-PC	Diamond Detectors Ltd [©]	CVD-D	300	Au : Au	$\varnothing 6.5$	100 : 100

2.3. Harsh environment

The global drive for continual data analysis of components and processes is leading the need for increasingly challenging detector requirements. One of the most difficult areas to address is for applications in harsh environments where sensitive detectors need to operate over wide temperature ranges, high pressures, large radiation fields or even under high mechanical stress.

Applications in the nuclear industry are often driven by temperatures up to several hundred degrees Celsius [18] and integrated neutron exposures up to 10^{18} n cm⁻² [19–21]. Significant ionizing photon radiation is also present, requiring both neutron–gamma discrimination and ionizing photon radiation hardness.

Within spacecraft and aerospace environments, integrated radiation doses are high due to solar flares and planetary magnetospheric radiation (>0.2 mSv d⁻¹ ambient dose equivalent [22, 23]), whereas mechanical stresses may be extensive during transit [3]. Detectors for automobile applications, particularly in engines, not only have to survive significant mechanical stress but also temperatures potentially up to 1000 °C [24].

In natural resource well logging (oil and gas) detection systems operate in environments up to ≈ 300 °C [4], pressures > 1000 atm and relatively large radiation doses due to the active interrogation method and background radiation from the rock. Detectors must also be able function after extreme mechanical stress when installed in drilling heads [25].

3. Experimental methods

3.1. Sample preparation

A summary of detectors under investigation is given in table 1. The D-SC detector was fabricated from Element Six Ltd[©] electronic grade CVD-D with 4×4 mm² platinum contacts [26] [27]. The D-PC detector was fabricated from Diamond Detectors Limited[©] CVD-D material with $\varnothing 6.5$ mm gold contacts [27, 28].

The SiC-EP detector was fabricated from Cree[©] material [29, 30] consisting of a $50 \mu\text{m}$ epitaxial layer of n-type 4H-SiC (5×10^{14} cm⁻³) grown on $360 \mu\text{m}$ of 4H-SiC bulk

semi-insulating substrate. Ti/Pt/Au Schottky contacts were applied and annealed to 1000 °C, whereas Ni/Au was used for the ohmic contacts.

As the radiation detection capabilities of epitaxial silicon carbide have been demonstrated in many works [31–34] it was decided that the *self-biased* (0V applied) radiation detection performance of the SiC-EP detector would be determined. This mode of operation is a particularly interesting concept for the applications discussed within this paper, as not only does it allow for reduced electronics and power consumption but the low bias results in smaller depletion regions (x_{det}) which could decrease the active volume but also potentially minimize gamma cross-sensitivity in the detectors [35], as shown by equation (1) [36]:

$$x_{\text{det}} \cong \sqrt{2\epsilon\epsilon_0 V \mu \rho_e}. \quad (1)$$

Here ϵ is the dielectric constant of the semiconductor material, ϵ_0 is the permittivity of free space, V is the bias, μ is the mobility of the majority charge carrier and ρ_e is the detector resistivity.

The SiC-SI detector was fabricated from Cree[©] 4H-SiC material with 5×5 mm² Ti/Pt/Au Schottky contacts and Ni/Au ohmic contacts [33]. Additional SiC-SI detectors were fabricated from $350 \mu\text{m}$ 4H-SiC (on-axis) Cree[©] material with Ti/Pt/Au Schottky contacts and Ni/Au ohmic contacts were sputter deposited onto the material over areas covering 9×9 mm² (Cr3), 2×2 mm² (Cr4) and 5×5 mm² (Cr5). Each sample was cleaned with isopropanol (heated to 85 °C), methanol (heated to 85 °C) and acetone (heated to 50 °C in an ultrasonic bath) prior to sputtering. For the Ni/Au ohmic contacts the samples were annealed to 150 °C for 60min and 980 °C for 2min in a MTI GSL-1100X tube furnace (10 °C/min heat/cool profile) with a constant flow of nitrogen gas. Similarly the Ti/Pt/Au Schottky contacts were annealed to 500 °C for 30 min using the same technique.

A commercial Hamamatsu[©] Si-PIN photodiode, type S1223-01, was used as a comparison benchmark. The standard package window was carefully removed in order that the detector could be utilized for alpha and beta detection, as demonstrated by Gooda and Gilboay [37].

3.2. Dark leakage current

The current–voltage (I – V) relationship of each detector was determined using a combined Keithley 487 picoammeter and voltage supply in series with a 10 k Ω resistor. Each test was conducted within a light-sealed diecast metal test box at room temperature (≈ 22 °C), with each voltage increment given up to 100 s to stabilize before being read.

Between 0 V and the ± 5 V region the current was measured for ± 0.1 V increments so as to give the best representation of the bulk resistivity of the material. At higher biases the surface impurities and the contact materials dictate that the resistivity be measured across an interfacial layer between the semiconductor and the metal contact as a result of variations in the space-charge region [38, 39]. The work of Bolotnikov *et al* has shown that this region subtends ± 1 V in CdZnTe semiconductor detectors [38, 39], but the concept can be applied to other high-resistivity materials as well.

From the straight-line fit of the I – V relationship, the gradient relates to the resistance (R) and the resistivity (ρ_e) of a semiconductor detector of thickness x , given by

$$\rho_e = \frac{a}{x} \quad (2)$$

where a is the area of the contact. This equation assumes that the leakage current is 0 A at 0 V bias and that the detector is a simple parallel electrode detector. In reality this is not always the case when measuring fully fabricated detectors (rather than just the material), due to variations caused by fabrication and slight offsets in the measuring equipment at the very low currents measured. However, even in these circumstances, equation (2) still operates as a good and simple figure-of-merit check for the resistivity of the material.

3.3. Radiation spectroscopy

For all radiation-based testing the detectors were mounted within a light-sealed diecast metal test box and connected to ORTEC 142A charge-sensitive preamplifiers, ORTEC 570 or 572 shaping amplifiers, an ORTEC 710 quad-bias supply and an ORTEC Easy-MCA multi-channel analyser (MCA) with associated Maestro software. Energy calibration of the detectors was conducted using pulser–capacitor calibrations as described by Siegbahn [40]:

$$E_{\text{pulser}} = V_{\text{pulser}} \times W \times C_{\text{cap}} \quad (3)$$

(keV) (mV) (eV) (pF)

where E_{pulser} is the equivalent energy deposited into the electronics system, V_{pulser} is the amplitude of the input pulser peak, W is the average electron–hole creation energy for a given material and C_{cap} is the capacitance value of a capacitor connected in series with a preamplifier and pulser. By plotting E_{pulser} against the resultant peak centroid position on the MCA output, a linear relationship can be observed, the equation of which gives the calibration factor for the detection system.

The D–SC, D–PC and SiC–SI detectors have all demonstrated some form of the so-called *polarization effect* during

irradiation, i.e. a change in the acquired spectrum and/or count rate with time [27, 41–43]. This particular effect is prevalent in low-doped, wide-bandgap semiconductors (D [44], SiC [45], CdZnTe [46] and CdTe [47]) and is a result of charge carriers being trapped for long periods of time, leading to a change in the space-charge distribution [36]. As such, between each radiation exposure the detectors were exposed to at least 15 min of room ambient light while at 0 V bias, in order to de-polarize the detector. This procedure was found to reset the peak position, count rate and polarization rate performance of the detectors with a reasonable level of repeatability.

For the applications discussed, the detector must be able to detect neutrons in a mixed-field environment. Most neutron sources result in ionizing photon and neutron fields, but reactions with the surrounding environment mean that charged particles are also likely to be present in a high-energy neutron field and should be considered.

In order to detect neutrons within this environment the detector should either be insensitive to the interference radiation or be able to discriminate against it. As such, the detectors were tested over the standard range of radiation types (alpha, beta, x-ray, gamma, neutron) in order to characterize their susceptibility.

All alpha spectra tests were conducted with a 3.7 kBq Am-241 source (5.485 MeV) inside a vacuum chamber at a pressure of 8×10^{-2} mbar. Alpha polarization testing was conducted in air with a 60 kBq Am-241 source (actual emission at 3.976 MeV). Similarly, beta irradiations were conducted in air with 178 kBq Sr-90/Y-90 source (0.544 MeV/2.270 MeV).

X-ray and gamma-ray irradiations were conducted at AWE using either a Pantak x-ray generator with ISO 4037 narrow spectrum filtration [48] or a gamma irradiator with Cs-137 (0.6617 MeV) or Co-60 (1.1732 MeV, 1.3325 MeV) sources of various activities. Unless otherwise stated, the ionizing photon ambient dose equivalent rates were ≈ 6 mSv h $^{-1}$.

Mono-energetic neutron exposures were conducted at the National Physical Laboratory (NPL). Radionuclide neutron exposures (Cf-252, AmBe) were conducted at NPL, AWE and Thermo Fisher Scientific (Beenham, Reading, UK). Where possible these tests were conducted in ambient dose equivalent fields greater than 6 mSv h $^{-1}$ and irradiated for times exceeding 2 h in order to obtain reasonable counting statistics in all channels. For mono-energetic 16.5 MeV neutrons the data presented uses the standard calibration setting, and as such the end-point energy is reduced.

Before every irradiation the detectors were exposed to at least 15 min of room ambient light while at 0 V bias, in order to remove any polarization within the detector.

3.4. Fast neutron convertor layers

The most statistically probable interaction method for fast neutrons is elastic recoil scattering where the incident neutron transfers a portion of its kinetic energy to the absorbing material through direct collisions.

Elastic interactions result in a change of direction and energy for the incident neutron as well as a gain of energy and momentum for the nucleus which recoils. If the energy transferred to this nucleus is such that its velocity is greater than that of its orbital electrons, it will lose those electrons and move through the medium as a heavy charged particle.

As discussed by Knoll [36], the maximum transfer of energy between the incident neutron and target nucleus occurs when the scattering angle of the incident neutron is 180° or the recoil angle of the nucleus is 0° . However, the energy transfer is fundamentally limited by the atomic mass of the absorber nuclei (A), as given by equation (4) [36]:

$$E_r = \frac{4A}{(1+A)^2} (\cos^2\theta) E_n \quad (4)$$

where E_r and θ are the recoil energy and angle of the nucleus respectively.

For carbon and silicon the maximum relative energy conversion ratio (E_r/E_n) of the incident neutron (E_n) and the nucleus are 0.28 and 0.13, respectively, allowing for potential use as a direct neutron detector [27].

However, for hydrogen the limit is 1.0, due to its similar mass relative to a neutron, making it theoretically possible for complete neutron energy transfer following collisions. For this reason hydrogenous materials such as water or plastic are by far the most popular media for neutron shielding and moderation. Hydrogenous materials can also be used for direct detection (such as proton recoil detectors) or for conversion detection, where the recoil hydrogen atom (proton) is detected by a charged particle detector [33, 49–52].

Subject to the fast neutron energies, the potential energy of these *conversion protons* is high and as such it is possible the penetration depth will be more than the thickness of the detector (a 16.5 MeV proton could travel ≈ 1.7 mm in Si or C [53]). Similarly if the convertor layer is too thick, the conversion protons may not escape and fast neutrons will be attenuated. Furthermore, it is also possible that the conversion protons will be emitted at non-incident angles, depositing a fraction of their energy or not even hitting the detector. Consequently, the addition of any form of conversion layer will result in a maximum intrinsic efficiency limited by the sequence of probabilities for interaction and detection [5].

Within this investigation a piece of Kapton $25\ \mu\text{m}$ thick was used as a hydrogenous convertor layer to study the efficiency and operational stability of this detection modality. The distance from convertor layer to the detector varied from detector to detector due to the arc of the bonding wire (the two could not touch due to the Kapton adhesive), but it was generally around 1–2 mm.

3.5. Temperature testing

Temperature testing was limited to detectors mounted on small ceramic boards and conducted in a vacuum cryostat from $-60\ ^\circ\text{C}$ and $+100\ ^\circ\text{C}$ (213 K to 373 K) with the 60 kBq Am-241 source. The boards with detectors were secured on

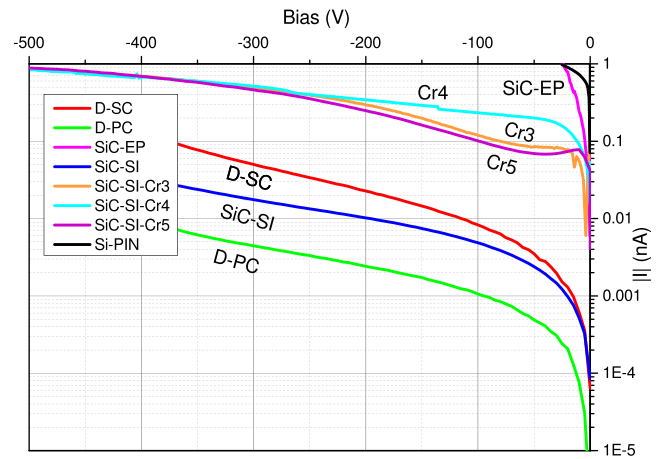


Figure 1. Current magnitude against voltage, normalized to the 0V inflection point. The settling time following bias change was 1 s, with 10 samples taken at each bias. SiC–SI–Cr3, SiC–SI–Cr4 and SiC–SI–Cr5 are Cree semi-insulating SiC detectors with contact sizes 9×9 mm, 2×2 mm and 5×5 mm, respectively.

the heat/cool plate within the cryostat using thermal coupling paste and a physical latch. A thermistor was also placed within the cryostat such that it was in contact with the ceramic board and therefore acted as a direct check of the temperature of the detector during testing. The preamp, shaping amp, bias supply and MCA were all outside the vacuum cryostat and not subject to the temperature variations.

Due to the mounting of the SiC–SI and Si–PIN detectors (PCB), as well as the size of the D–PC detector, this testing was limited to the D–SC and SiC–EP detectors, as well as the SiC–SI–Cr5 sample, which was deemed a suitable substitution for the SiC–SI detector.

The cryostat was pumped down to a vacuum of 6.4×10^{-1} mbar for all tests conducted. The heat/cool plate was connected to either an Oxford Instrument ITC 503 or Mercury ITC, subject to the requirement of cooling or heating, respectively, as described in [4]. For cooling, a supply of liquid nitrogen was pumped throughout the system, with the temperature automatically regulated by the ITC 503 instrument.

4. Results

4.1. Dark leakage current

The I – V characteristics of the detectors are shown in figure 1, as well as for the three samples of Cree semi-insulating material with different size contacts (SiC–SI–Cr3, SiC–SI–Cr4, SiC–SI–Cr5). In addition to this, the resistivities of the diamond detectors and SiC–SI are given in table 2. The resistivities of the SiC–EP and Si–PIN detectors were not determined as the more complex doping and contact arrangement did not reflect the simplified geometry required for equation (2).

All the detectors under test showed very good leakage currents over the ranges tested, of the order of nA, which would suggest good operation for most radiation detection applications [36], in particular particle detection and electronic personal dosimetry.

Table 2. Key performance criteria of the detectors under test. The leakage current density was taken at the typical operating bias. Operational characteristics of D–SC, D–PC and SiC–SI detectors have been demonstrated in [27].

Detector	Typical operating bias (V)	Leakage current density (nA cm ⁻²)	Resistivity (Ω cm)
Si–PIN	–25	–8.0 ± 0.1	—
SiC–EP	0	–6560 ± 1	—
SiC–SI	–400	–0.08 ± 0.02	0.53 ± 0.01 × 10 ¹³
SiC–SI–Cr3	–400	–0.8 ± 0.1	5.8 ± 0.1 × 10 ¹³
SiC–SI–Cr4	–400	–4.2 ± 0.1	12 ± 2 × 10 ¹³
SiC–SI–Cr5	–400	–2.7 ± 0.1	0.44 ± 0.01 × 10 ¹³
D–SC	–200	–0.077 ± 0.009	7.1 ± 0.2 × 10 ¹²
D–PC	–400	–0.011 ± 0.003	2 ± 1 × 10 ¹⁵

As would be expected for a wide-bandgap, low-intrinsic-carrier-concentration detector, the diamond samples demonstrated the lowest leakage current over the range of biases tested. The D–PC detector provided a lower and more stable leakage current than the D–SC, which is a reasonable observation when considering the calculated resistivities of the two materials: $2 \pm 1 \times 10^{15} \Omega \cdot \text{cm}$ compared with $7.1 \pm 0.2 \times 10^{12} \Omega \cdot \text{cm}$, respectively. It should be noted that the larger error in the D–PC value is a result of the observed low leakage currents over the tested range ($\pm 5\text{V}$) being at the limits of detectability of the picoammeter, namely of the order of fA.

The doped detectors (SiC–EP, Si–PIN) had higher leakage currents relative to the other detectors, as would be expected for the intentional increase in carrier concentration due to doping.

Comparisons of the three semi-insulating SiC Cree detectors (SiC–SI–Cr3, SiC–SI–Cr4, SiC–SI–Cr5) show that the leakage currents are of a similar order of magnitude, particularly at high operating voltages, despite the different contact areas.

For active interrogation and electronic personal neutron dosimetry applications, these observations are of particular interest as it suggests that low-noise, larger-area detectors are possible. These results also validate the fabrication technique used (i.e. little variation from detector to detector), although comparison between SiC–SI and SiC–SI–Cr5 suggests that the fabrication technique for the SiC–SI–Cr detectors could be improved further. Both these detectors were made from Cree material with similar resistivities and had the same contact area, but at higher biases the SiC–SI–Cr detector leakage currents are an order of magnitude greater.

The measured resistivity of the D–PC samples was similar to that of the published values by Schirru *et al* ($1.4 \times 10^{15} \Omega \text{ cm}$) [28] when considering the uncertainties.

The resistance at a given bias (+220V) for the D–SC sample was $0.76 \pm 0.06 \times 10^{14} \Omega$ compared to $2.2 \times 10^{14} \Omega$ as published by Abdel-Rahman *et al* [26]; however, as no guard ring was utilized in these detectors, leakage currents may have been influenced by surface effects.

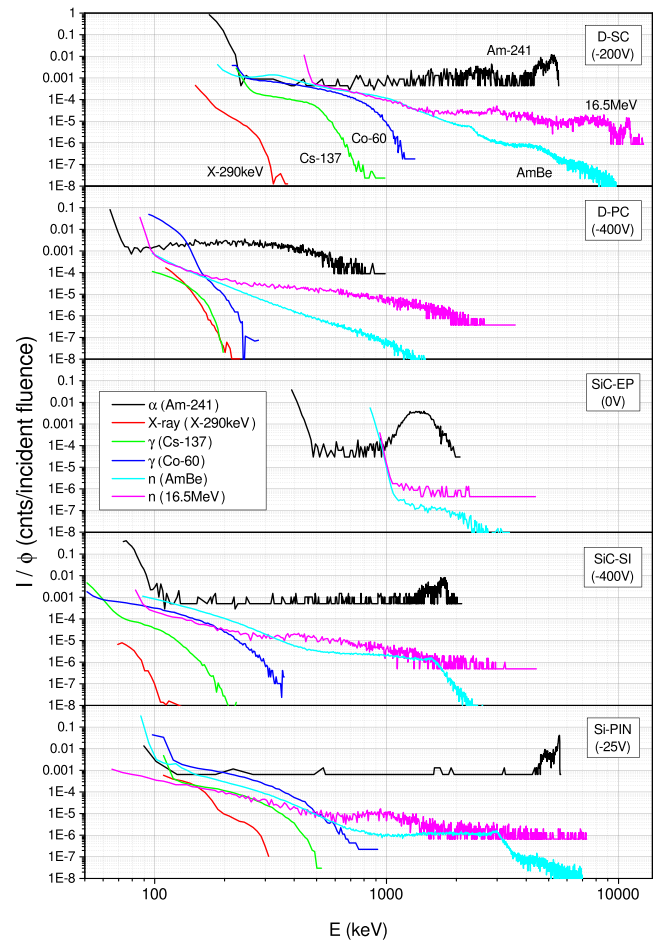


Figure 2. Count rate (I), normalized to incident flux (ϕ), against energy (E) as a function of alpha, x-ray, gamma, radionuclide neutron and mono-energetic neutron sources. Non-alpha data were taken at $\geq 6\text{mSv h}^{-1}$. The perceived ‘levels’ in some spectra (particularly alpha) are artefacts of the flux normalization and are associated with the detector’s ability to detect that radiation type. The calibration for the 16.5 MeV neutrons was optimized for low energies, resulting in a high-level threshold at $<16.5 \text{ MeV}$ for the detectors under test.

The leakage current of the SiC–EP detector was similar to that reported by Bruzzi *et al* in the RD50 collaboration [29] ($<10 \text{ nA}$ at -100 V). Si–PIN also performed as per the manufacturer’s expected leakage current response ($\approx 0.1 \text{ nA}$ at -10 V).

4.2. Radiation spectroscopy

Figure 2 shows the spectral response of each detector to multiple radiation types. Each spectrum has been normalized to the incident radiation flux. This type of normalization gives an indication of the relative sensitivities for each radiation type. For example, the vertical axis position of the alpha radiation data in the graphs is higher than for other radiation types, representing more counts per incident radiation particle. This is reasonable considering the large energy and shallow penetration depth of alpha particles, meaning that all of the incident particle’s energy will be transferred to the detector.

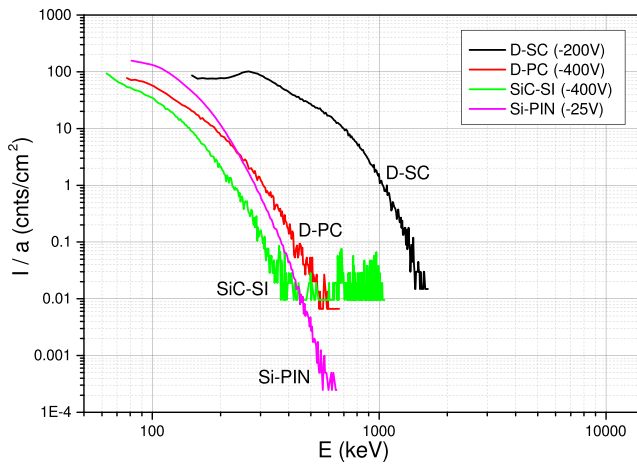


Figure 3. Count rate (I), normalized to contact surface area (a), against energy (E) for a $^{90}\text{Sr}/^{90}\text{Y}$ beta source. All spectra were taken in air.

The incident flux of the alpha sources were determined through the finite source approximation described by Knoll [36] and Ruby [54], with consideration given to self-attenuation losses. For x-ray and gamma-ray exposures the incident flux calculation utilized the calibrated dose rate from the test facilities and conversion factors taken the ISO 4037 series [48]. The incident flux of the neutron sources was calculated by the test house, where applicable.

Normalization to the incident flux was not possible for the beta radiation source as insufficient information was available on the surface emission rate and the tests were conducted in air due to safety pressure restrictions on the source. However, the data presented in figure 3 have been normalised to the contact surface area. As the detector-to-source distance was similar for most detectors, this normalization is proportional to the incident flux when comparing detectors.

A similar issue occurs when considering neutron conversion layers, as the true number of particles incident upon the detector includes scattered recoil particles and neutrons, as well as unscattered neutrons. Consequently the data have been plotted separately in figure 4 for D-SC and the intrinsic detection efficiency (total counts/total incident particles) is shown in table 3.

The results presented in figure 2 clearly show that all the detectors are capable of discriminating between each of the radiation types and energies tested using a simple energy threshold/discriminator method. This is particularly important for active interrogation applications when comparing the Co-60 gamma and AmBe neutron spectra, as the average energies for these two sources (1.2 MeV and 4.1 MeV) are similar to those found following fission [55].

When considering charged particles (alpha and beta) the region for direct neutron detection above the threshold level reduces for SiC-EP, SiC-SI and Si-PIN. For D-SC and D-PC the neutron detection capabilities above the alpha and beta thresholds remain very good.

There is little difference between the neutron detection capabilities of the Si-PIN and SiC-SI detectors, although as presented in table 4 comparison of the different neutron

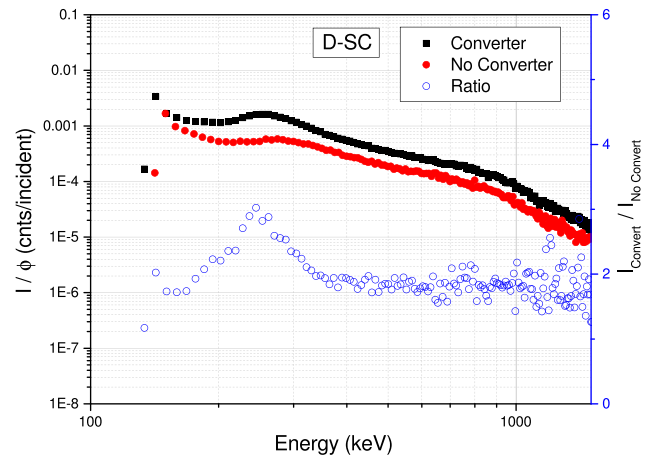


Figure 4. Count rate (I), normalized to incident flux (ϕ), against energy (E) for a D-SC detector irradiated with the AWE AmBe neutron source ($\approx 6\text{mSv h}^{-1}$) at -200 V . The converter is a $25\ \mu\text{m}$ Kapton layer. The ratio of counts per channel with (I_{Convert}) and without ($I_{\text{No Convert}}$) converter layer has also been plotted as a function of energy.

Table 3. Calculated intrinsic efficiencies for detectors under irradiation of an AmBe neutron source ($\approx 6\text{ mSv h}^{-1}$), with and without a $25\ \mu\text{m}$ Kapton converter layer.

Detector	Intrinsic efficiency		
	No converter (%)	Converter	Error
D-SC	2.59	5.35%	$\pm 0.01\%$
D-PC	2.234	—	$\pm 0.004\%$
SiC-EP	0.010	0.011%	± 0.002
SiC-SI	0.42	1.26%	$\pm 0.04\%$
Si-PIN	0.78	2.63%	$\pm 0.04\%$

end-point energies (E_{max}) showed that both SiC detectors had very good neutron energy discrimination ability [$E_{\text{max}}(5\text{ MeV})/E_{\text{max}}(1\text{ MeV}) \approx 5$]. For Si-PIN discrimination was still possible, but to a lower extent [$E_{\text{max}}(5\text{ MeV})/E_{\text{max}}(1\text{ MeV}) \approx 2$].

Despite demonstrating the highest intrinsic neutron efficiencies (table 3), highlighting the advantage of direct carbon-neutron recoil reactions, both the D-SC and D-PC detectors gave a lower neutron energy discrimination ratio, with $E_{\text{max}}(5\text{ MeV})/E_{\text{max}}(1\text{ MeV}) \approx 3.5$ and 2.5 , respectively.

The D-PC detector did provided the best gamma cross-sensitivity ratio ($E_{\text{max}}(\text{AmBe})/E_{\text{max}}(\text{Co-60}) \approx 16$) due to the low gamma interaction probability (Z) of the material. D-SC would be expected to perform similarly but the detector was thicker ($500\ \mu\text{m}$ compared with $300\ \mu\text{m}$) and as such had a lower neutron/gamma ratio (8.1) due to an increased gamma interaction probability. Similarly the thicker detector led to an observed ‘peak’ in the $^{90}\text{Sr}/^{90}\text{Y}$ beta spectrum (figure 3) attributed to ^{90}Sr emissions ($E_{\text{max}}(\text{Sr-90}) = 0.546\text{ MeV}$) when losses due to air are considered.

4.3. Gamma and neutron intrinsic efficiency

Using the results presented in table 1, the intrinsic efficiency has been normalized to the depletion width (calculated from

Table 4. Summary of key findings. The cost per unit efficiency is given by $\mathcal{L}/\epsilon_i(\text{AmBe})$ and was derived from wafer costs following conversations with suppliers; additional processing has not been included.

Detector	Bias	Neutron discrimination	Cross-sensitivity	$\mathcal{L} \text{ mm}^{-2}$	$\mathcal{L} \epsilon_i$ (AmBe)
		$\left(\frac{E_{\max}(5 \text{ MeV neutrons})}{E_{\max}(1 \text{ MeV neutrons})}\right)$	$\left(\frac{E_{\max}(\text{AmBe})}{E_{\max}(\text{Co-60})}\right)$		
D-SC	−200 V	3.5	8.1	98.76	900
D-PC	−400 V	2.5	16.0	3.43	1334
SiC-EP	0 V	5.0 ^a	6.4	3.40	3×10^6
SiC-SI	−400 V	4.9	6.9	0.59	4206
Si-PIN	−25 V	2.0 ^a	9.1	0.02	284

^a Denotes neutron energy discrimination determined from the ratio of AmBe and Cf-252, $E_{\max}(\text{AmBe})/E_{\max}(\text{Cf} - 252)$.

capacitance measurements) in figure 5 for gamma and neutron energies. This could effectively be regarded as the detection efficiency per unit of active volume for a detector, a very important factor when considering the overall design, cost and eventual scaling for the applications discussed.

Taking the thickness of the detector region into consideration shows that D-SC actually provides the lowest intrinsic efficiency for low-energy ionizing photons as per figure 5.

The SiC-EP detector is quite insensitive to gamma radiation, as would be expected from the low Z number and narrow depletion width in self-biased operation. Furthermore the calibration setup of the detector is such the noise edge (the point at which electronic noise in the system produces a non-negligible number of counts in the absence of a radiation source) was at least at 0.750 MeV with a slightly higher noise edge used during neutron testing (≈ 1 MeV) due to increased noise in the system. Although an order of magnitude larger than the gamma intrinsic efficiency, the neutron efficiency is also quite low in this detector, but this could feasibly be compensated for in large-area applications with a combined array of detectors.

Similarly the SiC-SI detector demonstrated a lower overall gamma sensitivity relative to Si-PIN (figure 5), which would be expected for the lower atomic number (Z) of the material. However, both SiC-EP and SiC-SI detectors actually demonstrated the lowest gamma cross-sensitivity ratios relative to Co-60 (6.4 and 6.9, respectively).

Although the direct neutron detection capability of Si-PIN has been shown to be comparable, the reduced overall gamma sensitivity of the carbon-based detectors ensures that lower energy thresholds can be used, allowing for a more sensitive neutron detector. These results are of particular importance for electronic personal neutron dosimetry applications, where a reduced neutron-gamma cross-sensitivity leads to lower detector thresholds and a potentially improved energy response.

It is worth noting that in figure 5, the radionuclide sources (highlighted in the graphs) have been plotted using their average energy. For mono-energetic neutron sources the emission energy is very well defined, with some facilities capable of determining energies to within $\pm 1.5\%$. For radionuclide sources, however, there is a very wide range of neutron energies emitted due to the complex nature of the interactions occurring. With Cf-252 and AmBe radioisotope neutron sources, for example, despite having an average energy of 2.1 MeV and 4.1 MeV, neutrons can be emitted with energies ranging

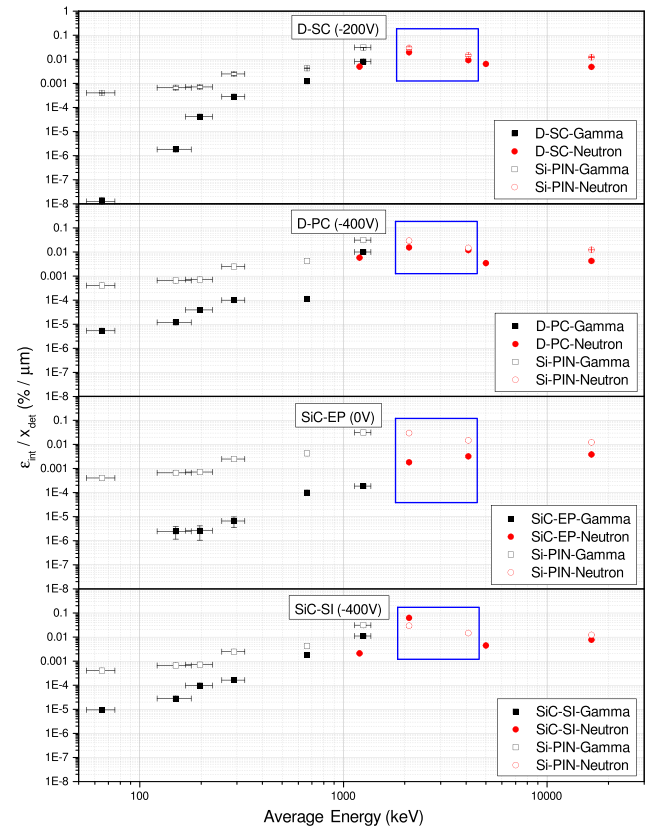


Figure 5. Depletion thickness compensated for intrinsic efficiency ($\epsilon_{\text{int}}/x_{\text{det}}$) against energy for x-rays, gamma-rays and mono-energetic neutrons (1.2 MeV, 5.0 MeV, 16.5 MeV). The highlighted area shows the average neutron energy emissions for the radionuclide sources (Cf-252 = 2.1 MeV, AmBe = 4.1 MeV). All data were acquired at $\approx 6 \text{ mSv h}^{-1}$.

up to 15 MeV and 11 MeV, respectively [56]; however, for comparative purposes the average energies are included.

4.4. Fast neutron convertor layers

The benefit of a hydrogenous convertor layer has been demonstrated in figure 4 and table 3, with clear increases in the intrinsic efficiency for D-SC, SiC-SI and Si-PIN by factors of two- to three-fold.

There was no significant improvement in the SiC-EP but this was to be expected due to the very thin depletion width when the applied bias is 0V (1.3 μm from table 1), as well as the large penetration depths of the conversion protons

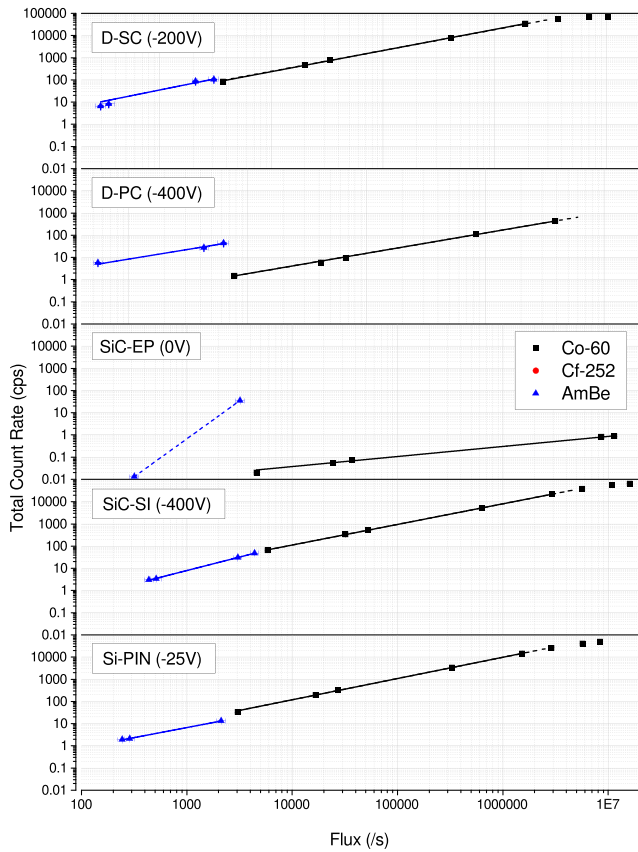


Figure 6. Total count rate above a given threshold against incident radiation flux for Co-60 gamma radiation and AmBe neutron radiation. The dashed line represents non-linear operation caused by pulse pileup in the MCA; for the SiC-EP detector this was a result of noise alone.

(18 μm from SRIM [53]). The application of the conversion layer was particularly difficult for the D-PC detector due to a large bonding wire and subsequent increased distance between the layer and detector; as such the measurement could not be made.

4.5. Dose rate dependence

As can be seen in figure 6 the performance of these detectors is maintained over a wide dynamic range of neutron and gamma fluxes. This shows that the data are a result of direct gamma and neutron detection and not electronic noise or interference as the counting efficiencies are only dependent upon the radiation dose received. At very high fluxes the count rate becomes non-linear due to pulse pileup within the MCA.

4.6. Polarization effects

With the exception of SiC-EP and Si-PIN, all the detectors demonstrated a change in the acquired spectrum and/or count rate with time, the so-called *polarization effect* [44, 45].

This is a result of charge carriers being trapped in deep-level locations for long periods of time, leading to a change in the space-charge region, and is very dependent upon the density of ionization within the detectors, with radiation that results

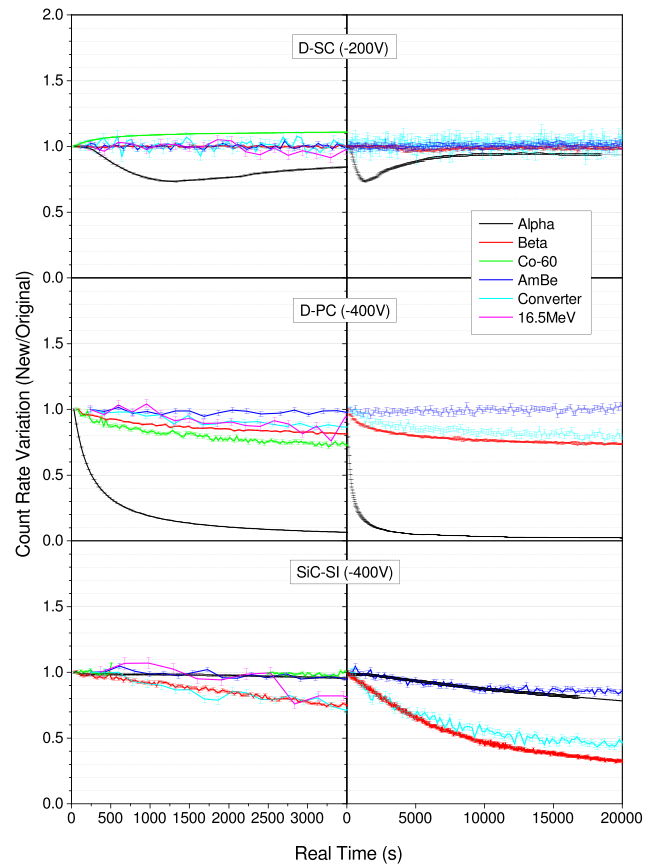


Figure 7. Count rate variation (I/I_0) against time as a function of radiation type. Tests were conducted over 3600 s and 20000 s. The alpha source was Am-241 (185 kBq) in an 8×10^{-2} mbar vacuum. AmBe was $\approx 18 \text{ mSv h}^{-1}$, whereas the converter represents the AmBe neutron irradiation at $\approx 6 \text{ mSv h}^{-1}$ with a 25 μm Kapton proton conversion layer. Co-60 gamma and 16.5 MeV neutron data were taken at $\approx 6 \text{ mSv h}^{-1}$.

in a large ionization concentrations in a small volume (such as alpha particles) producing very quick polarization effects, as demonstrated in figure 7. This is because these particles tend to create a large concentration of charge carriers at shallow depths within the detector ($\approx 17 \mu\text{m}$ for diamond and $\approx 18 \mu\text{m}$ for SiC [53]), resulting in a high trapping rate over a small region [41–43]. This leads to the creation of a localized space-charge barrier close to the electrode, through which further electrons and holes must pass to be fully collected.

A stable count rate was observed for the D-SC detector during beta, neutron and neutron plus conversion proton irradiations, suggesting no polarization. This is to be expected, as these radiation types would result in less ionization per incident radiation particle and therefore less trapping.

Furthermore, a more uniform creation of electron-hole pairs across the detector thickness would be expected for these radiation types, resulting in the trapped charges being distributed more evenly, diluting the overall space-charge build-up and reducing the polarization effect [57].

Interestingly, for D-SC, the Co-60 gamma irradiation has been shown to actually increase the count rate and effectively *enhance* the detection capability, whereas alpha polarization has been shown to recover over longer time periods. These

observations demonstrate *priming*, whereby the traps within the material are steadily filled with the created charge carriers until they reach saturation point, after which a stable field, and therefore spectrum, is maintained [42, 57].

For the alpha particles the count rate initially decreases as initial charge carriers are trapped and incomplete charge collection in the detector occurs, resulting in some of the created pulse being less than the discriminator level. As the traps reach saturation, further charge carriers are again able to fully traverse the detector, resulting in the count rate returning to normal and stabilizing, demonstrating *shallow* priming. However, it should also be noted that the trapped charges do create an additional space-charge barrier, inhibiting the movement of further charge carriers and resulting in an observed reduced, but stable, alpha energy peak position.

The Co-60 irradiation on the other hand demonstrates *uniform* priming, where initial charge carriers fill traps within the material leading to incomplete charge collection and an initial low count rate. However, future charge carriers can more easily traverse the material without being trapped and so the count rate will increase. As the trapped charge is evenly distributed throughout the detector there is not a localized space-charge barrier for the charge carrier to overcome and there is little or no effect on the spectral position.

The quality of the D-SC material is such that the number of traps is significantly less than the rate of charge generation; essentially traps are rapidly filled and equilibrium is reached quickly. For D-PC and SiC-SI it is clear from figure 7 that there are significantly more trap sites within the material as equilibrium is not reached and polarization is observed for nearly all exposures.

As would be expected, the polarization rate is very dependent upon the ionization density of each radiation type and the distribution of the created charge carriers in the detector. In general, alpha particles show the greatest polarization rate (high energy, full deposition of energy in material, highly concentrated charge carrier creation), followed by beta particles (lower energy, higher penetration) and then conversion protons (lower stopping power, higher penetration subject to the incident neutron energy).

For alpha particles in particular, the polarization tends towards debilitating effects within D-PC as the spectra move into the noise region and no further pulses can be registered. This is primarily due to the large emission rate of this source and the shallow penetration depth. This effect is not as apparent within the SiC-SI data, despite being demonstrated previously [27]. This is probably due to these exposures being conducted in air, resulting in a lower incident flux upon the detector which would be closer to the trapping/detrapping equilibrium.

Generally, polarization (rather than priming) seems to dominate when charge carriers are not generated throughout the whole active thickness of the device.

For the D-PC detector a stable count rate was observed for the AmBe neutron exposure, despite the SiC-SI detector showing a polarization effect for the same exposure. As the D-PC detector had a larger area, it is possible that this is simply an effect of a reduced ionization concentration over

the whole detector (i.e. for the same dose rate, the flux at the boundary of D-PC will be less than for SiC-SI). As such the reduced uniform trapping rate throughout the detector would be closer to equilibrium with the detrapping rate, resulting in no observable net polarization effect. Certainly neutron polarization has been observed in D-PC using a very high flux Cf-252 neutrons with the same principle [27].

It is also possible that this effect could be related to the enclosures in which the detectors were tested, with the D-PC enclosure likely to produce more scattered electrons from Co-60 exposure (polarization observed) and the SiC-SI enclosure likely to produce more recoil particles from neutron exposure (polarization observed). These effects could be avoided in future testing by placing a low-Z filter (e.g. Al) between the source holders and detector to absorb the conversion particles, a common feature in radiation detection instrumentation.

It is worth noting that despite the onset of polarization effects operation was still possible for all detectors, with the potential exception of the alpha source exposures. For the diamond detectors in particular the count rate rapidly stabilizes following irradiation, demonstrating the point at which trapping and de-trapping are in equilibrium. As such, all the detectors may be suitable for use in the applications discussed with suitable polarization management techniques [43, 58–63].

In fact, the selection of detectors for a particular application should be carefully considered. Diamond detectors are often considered to be quite expensive, as shown for the cost per unit area in table 4. However, for direct neutron detection the cost is actually comparable to the cheaper Si-PIN material when considering the relative efficiency. Furthermore, although Si-PIN detectors are not naturally thought of as direct neutron detectors Si-PIN detectors have been shown to be cheapest detector overall—essentially they detect more neutrons per pound sterling than the alternatives tested.

4.7. Temperature

The effect of temperature on the alpha detection capability of SiC-EP, SiC-SI and D-SC has been shown in figure 8. It was observed that the alpha detection characteristics of the D-SC detector are constant over all temperatures tested up until 373 K, at which the peak position reduces by around 60% and the full-width at half-maximum doubles.

For the SiC-SI detector there are variations in the alpha peak position (P_T) with all temperatures tested, although the detector remains capable of detection at each point. It is also interesting to note that the maximum peak position (P_{\max}) is achieved at room temperature (293 K). Altering the temperature by ± 40 K reduces the peak position by ≈ 40 –45%, and altering the temperature by ± 80 K by decreasing the peak by ≈ 40 –55%, suggesting a Gaussian-style relationship of the order

$$\frac{P_T}{P_{\max}} = y_0 + \left(\frac{A}{w\sqrt{\pi/2}} \right) \cdot e^{-2((T-x_c)/w)^2} \quad (5)$$

where T is the temperature. The values y_0 , A , w and x_c are all constants derived from the Origin software using a

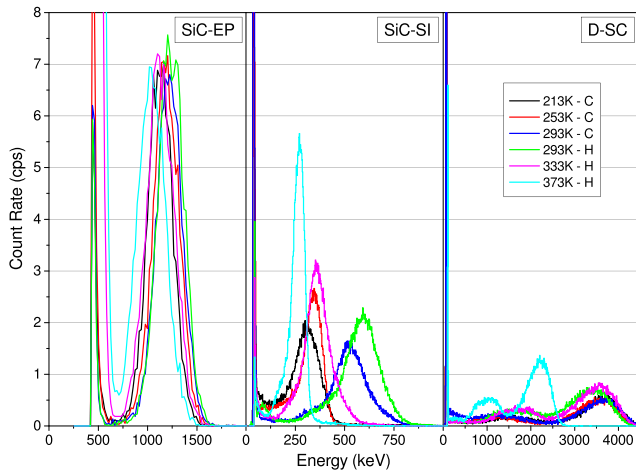


Figure 8. Count rate against energy as a function of temperature for a 60 kBq Am-241 alpha radiation source. Suffixes ‘C’ and ‘H’ represent the cryostat used for cooling and heating, respectively. Data were taken at 293 K in both cryostats for comparison. All testing was conducted at 6.4×10^{-1} mbar.

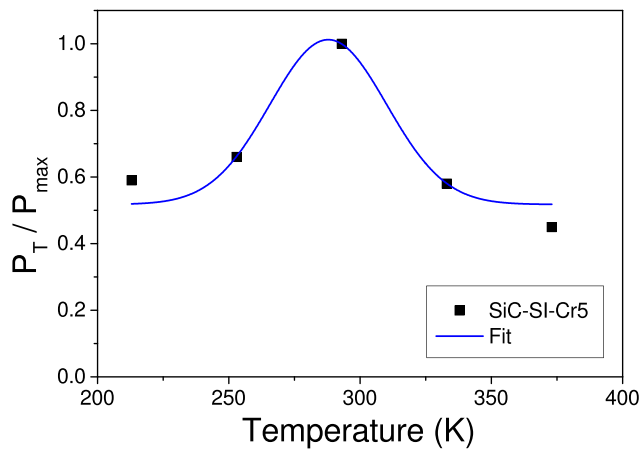


Figure 9. Variation of peak position (P_T) relative to position at 293 K (P_{\max}) as a function of temperature for SiC-SI-Cr5 at -400 V applied bias. The fit is an Origin Gaussian function using Levenberg–Marquardt empirical iterations.

Levenberg–Marquardt empirical iteration function [64], given by

$$\begin{aligned} y_0 &= 0.51 \pm 0.07 \\ A &= 287 \pm 9(\text{K}) \\ w &= 44 \pm 15(\text{K}) \\ x_c &= 27 \pm 11 \end{aligned}$$

but it is worth noting the R^2 fit is 0.77 due to non-symmetry at the extremes, as shown in figure 9.

For the self-biased SiC-EP detector there is little or no variation in the peak position or resolution over the range of temperature tested. Combined with the work presented by Abubakar *et al* [4], which takes SiC-EP up to 500 K, self-biased epitaxial SiC detectors seem very promising for applications in harsh environments (i.e. reduced electronics, intrinsically safe operation).

The leakage currents of the detectors while under bias increased with temperature as an exponential function ($\propto e^{\frac{-1}{T}}$)

but were still well within operational capabilities [36]. The leakage currents of the D-SC detector (at -200 V) varied from $I_{213\text{K}} \approx 0.1$ fA to $I_{373\text{K}} \approx 0.1$ nA and from $I_{213\text{K}} \approx 1$ fA to $I_{373\text{K}} < 10$ nA for the SiC-SI-Cr5 (at -400 V) detector. No significant variation in leakage current was observed for SiC-EP at (0V), but variation was more pronounced when under bias negative bias (\approx mA at -40 V).

5. Conclusion

A thorough investigation has been carried out in order to determine the suitability of diamond and SiC detectors for specialist neutron detection applications such as active interrogation, electronic personal neutron dosimetry and harsh environments. A complete set of radiation exposures including alpha, beta, x-ray, gamma, radionuclide neutron and mono-energetic neutrons have demonstrated the detection capabilities of epitaxial SiC (SiC-EP), semi-insulating SiC (SiC-SI), single crystal diamond (D-SC) and polycrystalline diamond (D-PC) over a wide dynamic range, with comparison against a commercial Si-PIN detector as a benchmark. Furthermore, the stability of the detectors while under radiation was shown, along with the performance of the SiC-EP, SiC-SI and D-SC detectors in temperatures ranging from -60 °C to $+100$ °C.

During the investigation stability issues were noted in the low-doped, wide-bandgap materials (D-SC, D-PC and SiC-SI detectors), namely a change of both peak position and count rate over time, the so-called *polarization effect*.

For D-SC, alpha radiation exposure caused an initial decrease in the count rate followed by a recovery to the initial rate, highlighting shallow priming, whereby all the traps are filled at a shallow location within the detector creating a space-charge barrier for future charge carriers. For Co-60 gamma-ray irradiations the count rate actually increased initially, followed by stable operation, demonstrating uniform priming by which all the traps are filled uniformly throughout the detector diluting the space-charge variation. For all other exposures the detector remained stable.

Polarization was observed in the D-PC and SiC-SI detectors for alpha, beta, gamma, radionuclide neutron (fast and thermal), mono-energetic neutron (fast) and neutron plus proton (converter) irradiations, with the exception of AmBe neutrons for D-PC and Co-60 gamma-rays for SiC-SI. The results obtained generally showed an increase in polarization rate as the ionization density of the incident particle increased (i.e. the number of charge carriers created per incident particle). For D-PC this was probably due to a lower overall incident flux relative to the other detectors as certainly radionuclide polarization has been demonstrated for higher Cf-252 fluxes [27].

Despite this, with the exception of the alpha irradiations, the polarization within the detectors was non-debilitating over the time period tested, and as such stable operation was possible after the initial change in performance.

Consequently, the detectors were shown to be able to directly detect and distinguish both the different radiation types and energies using a simple energy threshold discrimination method, with the SiC detectors demonstrating the best neutron

discrimination ratio and Si–PIN demonstrating the lowest ($E_{\max}(5 \text{ MeV neutrons})/E_{\max}(1 \text{ MeV neutrons}) \approx 5$ and 2, respectively). Essentially this ratio suggests it is easier to discriminate between the two neutron energies in SiC than in Si.

However, the SiC detectors did demonstrate the lowest neutron–gamma cross-sensitivity ratio relative to Co-60 photons ($E_{\max}(\text{AmBe})/E_{\max}(\text{Co-60}) \approx 6.5$), with D–PC providing the best ratio (16). This suggests that it could be more difficult to discriminate gamma-ray interference from direct neutron detection in SiC relative to the other detectors. Further work was presented showing that these cross-sensitivity ratios can be improved through use of a simple proton-recoil conversion layer and that the intrinsic gamma efficiency of the carbon-based detectors was less than that of the Si detector for lower-energy ionizing photons.

The work conducted also showed that SiC–EP could be used as an effective neutron detector when operated under self-bias. Neutron and alpha radiation could be clearly discriminated, whereas the intrinsic efficiency for ionizing photons was shown to be significantly lower than that of the other detectors due to the low Z number, narrow depletion width and calibration setup (i.e. low minimum energy threshold, $<0.750 \text{ kMeV}$).

Finally, work was conducted to demonstrate that SiC–EP, semi-insulating SiC and D–SC detectors could be operated in a wide range of environmental temperatures. Minor variations in alpha energy peak position were noticed for the SiC–Si and D–SC detectors, although detection capability was still maintained over $-60 \text{ }^\circ\text{C}$ to $+100 \text{ }^\circ\text{C}$. The self-biased SiC–EP detector on the other hand demonstrated no variation in alpha detection performance or quality for the range of temperatures tested.

Acknowledgments

The authors would like to acknowledge the staff at the University of Surrey, NPL, Thermo Fisher Scientific and AWE for their assistance with testing and analysis. The authors would also like to thank Loadpoint for their work during the detector fabrication process.

This work was funded by the United Kingdom Science Technology Funding Council (STFC grant number: ST/H003959/1) and in collaboration with AWE.

ORCID iDs

M Hodgson  <https://orcid.org/0000-0002-9013-7929>

References

- [1] Ruddy F H, Dulloo A R, Seidel J G, Das M K, Ryu S H and Agarwal A K 2006 The fast neutron response of 4h silicon carbide semiconductor radiation detectors *IEEE Trans. Nucl. Sci.* **53** 1666–70
- [2] Pillon M, Angelone M, Krása A, Plompen A J M, Schillebeeckx P and Sergi M L 2011 Experimental response functions of a single-crystal diamond detector for 5–20.5 MeV neutrons *Nucl. Instrum. Methods Phys. Res. A* **640** 185–91

- [3] Wrbanek J D, Wrbanek S Y, Fralick G C and Chen L-Y 2007 Micro-fabricated solid-state radiation detectors for active personal dosimetry *NASA Technical Report* 214674
- [4] Abubakar Y M, Lohstroh A and Sellin P J 2015 Stability of silicon carbide particle detector performance at elevated temperatures *IEEE Trans. Nucl. Sci.* **62** 2360–6
- [5] McGregor D S, Hammig M D, Yang Y-H, Gersch H K and Klann R T 2003 Design considerations for thin film coated semiconductor thermal neutron detectors—I: basics regarding alpha particle emitting neutron reactive films *Nucl. Instrum. Methods Phys. Res. A* **500** 272–308
- [6] Nava F, Bertuccio G, Cavallini A and Vittone E 2008 Silicon carbide and its use as a radiation detector material *Meas. Sci. Technol.* **19** 102001
- [7] Sellin P J and Vaitkus J 2006 New materials for radiation hard semiconductor detectors *Nucl. Instrum. Methods Phys. Res. A* **557** 479–89
- [8] Angelone M et al 2011 Spectrometric performances of monocrystalline artificial diamond detectors operated at high temperature *Nuclear Science Symposium Conference Record* (Piscataway, NJ: IEEE) pp 2188–91
- [9] Stevenson J, Gozani T, Elsalim M, Condon C and Brown C 2011 Linac based photofission inspection system employing novel detection concepts *Nucl. Instrum. Methods Phys. Res. A* **652** 124–8
- [10] Runkle R C, Chichester D L and Thompson S J 2011 Rattling nucleons: new developments in active interrogation of special nuclear material *Nucl. Instrum. Methods Phys. Res. A* **663** 75–95
- [11] Gozani T 2009 Fission signatures for nuclear material detection *IEEE Trans. Nucl. Sci.* **56** 736–41
- [12] Active Interrogation Project Requirements 2012 *Internal Report* Project Collaboration
- [13] Ginjaume M, Bolognese-Milsztajn T, Luszik-Bhadra M, Vanhavere F, Wahl W and Weeks A 2006 Overview of active personal dosimeters for individual monitoring in the European Union *Radiat. Prot. Dosim.* **125** 261–6
- [14] Chau Q and Lahaye T 2006 Evaluation of dose equivalent by the electronic personal dosimeter for neutron ‘SAPHYDOSE-n’ at different workplaces of nuclear facilities *Radiat. Prot. Dosim.* **125** 271–4
- [15] Luszik-Bhadra M, Matzke M, Dietz E, Guldbakke S, Hecker O, Sosaat W and Wiegel B 1999 An active personal dosimeter/spectrometer for neutrons *Radiat. Prot. Dosim.* **84** 375–80
- [16] Luszik-Bhadra M, Rosenfeld A, Kron T, d’Errico F and Moscovitch M 2011 State of the art in electronic dosimeters for neutrons *AIP Conf. Proc.* **1345** 262–73
- [17] d’Errico F, Luszik-Bhadra M and Lahaye T 2003 State of the art of electronic personal dosimeters for neutrons *Nucl. Instrum. Methods Phys. Res. A* **505** 411–4
- [18] Glasstone S and Sesonske A 1994 *Nuclear Reactor Engineering* 4th edn (New York: Chapman and Hall)
- [19] Steele L E 1975 Neutron irradiation embrittlement of reactor pressure vessel steels *International Atomic Energy Agency Technical Report* 163 (Vienna: IAEA)
- [20] IAEA 1990 Analysis and upgrade of instrumentation and control systems for the modernization of research reactors *IAEA TECDOC* 540 available from www.iaea.org/inis/collection/NCLCollectionStore/_Public/19/068/19068608.pdf
- [21] Health and Safety Executive 2017 Step 3 structural integrity assessment of the EDF and AREVA UK EPR *Division 6 Assessment Report* AR 09/012-P (Bootle: HSE Nuclear Directorate)
- [22] Luszik-Bhadra M, Matzke M and Schuhmacher H 2001 Development of personal neutron dosimeters at the PTB and first measurements in the space station MIR *Radiat. Meas.* **33** 305–12
- [23] Durante M 2014 Space radiation protection: destination Mars *Life Sci. Space Res.* **1** 2–9

- [24] Werner M R and Fahrner W R 2001 Review on materials, microsensors, systems and devices for high-temperature and harsh-environment applications *IEEE Trans. Ind. Electron.* **48** 249–57
- [25] Nikitin A and Bliven S 2010 Needs of well logging industry in new nuclear detectors *IEEE Nuclear Science Symp. and Medical Imaging Conf.* (IEEE) pp 1214–9
- [26] Abdel-Rahman M A E, Lohstroh A and Sellin P J 2011 The effect of annealing on the x-ray induced photocurrent characteristics of CVD diamond radiation detectors with different electrical contacts *Phys. Status Solidi a* **208** 2079–86
- [27] Hodgson M, Lohstroh A, Sellin P and Thomas D 2017 Neutron detection performance of silicon carbide and diamond detectors with incomplete charge collection properties *Nucl. Instrum. Methods Phys. Res. A* **847** 1–9
- [28] Schirru F et al 2012 Development of large area polycrystalline diamond detectors for fast timing application of high-energy heavy-ion beams *J. Instrum.* **7** P05005
- [29] Bruzzi M et al 2005 The SiC Common Structures project *7th RD50 Workshop (CERN, Geneva)*
- [30] Bruzzi M, Lagomarsino S, Nava F and Sciortino S 2003 Characterisation of epitaxial SiC Schottky barriers as particle detectors *Diam. Relat. Mater.* **12** 1205–8
- [31] Bertuccio G, Caccia S, Puglisi D and Macera D 2011 Advances in silicon carbide x-ray detectors *Nucl. Instrum. Methods Phys. Res. A* **652** 193–6
- [32] Bruzzi M, Nava F, Russo S, Sciortino S and Vanni P 2001 Characterisation of silicon carbide detectors response to electron and photon irradiation *Diam. Relat. Mater.* **10** 657–61
- [33] Ruddy F H, Seidel J G, Flammang R W, Singh R and Schroeder J 2008 Development of radiation detectors based on semi-insulating silicon carbide *IEEE Nuclear Science Symp. Conf. Record* pp 449–55
- [34] Nava F, Vanni P, Bruzzi M, Lagomarsino S, Sciortino S, Wagner G and Lanzieri C 2004 Minimum ionizing and alpha particles detectors based on epitaxial semiconductor silicon carbide *IEEE Trans. Nucl. Sci.* **51** 238–44
- [35] Ha J H, Kang S M, Park S H, Kim H S, Lee N H and Song T-Y 2009 A self-biased neutron detector based on an SiC semiconductor for a harsh environment *Appl. Radiat. Isot.* **67** 1204–7
- [36] Knoll G F 2010 *Radiation Detection, Measurement* 4th edn (New York: Wiley)
- [37] Gooda P H and Gilboy W B 1987 High resolution alpha spectroscopy with low cost photodiodes *Nucl. Instrum. Methods Phys. Res. A* **255** 222–4
- [38] Bolotnikov A E, Boggs S E, Hubert Chen C M, Cook W R, Harrison F A and Schindler S M 2002 Properties of Pt Schottky type contacts on high-resistivity CdZnTe detectors *Nucl. Instrum. Methods Phys. Res. A* **482** 395–407
- [39] Bolotnikov A E, Camarda G C, Wright G W and James R B 2005 Factors limiting the performance of CdZnTe detectors *IEEE Trans. Nucl. Sci.* **52** 589–98
- [40] Siegbahn K (ed) 1965 *Alpha-, Beta- and Gamma-Ray Spectroscopy* (Amsterdam: North-Holland)
- [41] Rogalla M, Runge K and Söldner-Rembold A 1999 Particle detectors based on semi-insulating silicon carbide *Nucl. Phys. B* **78** 516–20
- [42] Lan L, Xiaoping O, Xinjian T, Liangbin X, Na C, Bing L and Xiaodong Z 2012 Priming effect on a polycrystalline CVD diamond detector under 60-Co γ -rays irradiation *Nucl. Instrum. Methods Phys. Res. A* **672** 29–32
- [43] Lohstroh A, Sellin P J, Wang S G, Davies A W and Parkin J M 2007 Mapping of polarization and detrapping effects in synthetic single crystal chemical vapor deposited diamond by ion beam induced charge imaging *J. Appl. Phys.* **101** 063711
- [44] Chynoweth A G 1951 Behavior of space charge in diamond crystal counters under illumination. I *Phys. Rev.* **83** 54
- [45] Ivanov A M, Lebedev A A and Stokan N B 2006 Effect of extreme radiation fluences on parameters of SiC nuclear particle detectors *Semiconductors* **40** 1227–31
- [46] Camarda G S, Bolotnikov A E, Cui Y, Hossain A, Awadalla S A, Mackenzie J, Chen H and James R B 2008 Polarization studies of CdZnTe detectors using synchrotron x-ray radiation *IEEE Trans. Nucl. Sci.* **55** 3725–30
- [47] Siffert P, Berger J, Scharager C, Cornet A, Stuck R, Bell R O, Serreze H B and Wald F V 1976 Polarization in cadmium telluride nuclear radiation detectors *IEEE Trans. Nucl. Sci.* **23** 159–70
- [48] BS ISO 4037-3 1999 *X and Gamma Reference Radiation for Calibrating Dosimeters and Doserate Meters and for Determining their Response as a Function of Photon Energy. Calibration of Area and Personal Dosimeters and the Measurement of their Response as a Function of Energy and Angle of Incidence* (International Organization for Standardization)
- [49] Jones J L, Blackburn B W, Ruddy F H, Seidel J G and Flammang R W 2007 Novel silicon carbide detector for active inspections *Government Microcircuit Applications, Critical Technology Conf. (Orlando, FL)* (Idaho Falls, ID: Idaho National Laboratory)
- [50] Zat'ko B, Sedlačková K, Dubecký F, Boháček P, Sekáčová M and Nečas V 2011 Detection of fast neutrons using detectors based on semi-insulating GaAs *J. Instrum.* **6** C12047
- [51] Sasaki M, Nakamura T, Tsujimura N, Ueda O and Suzuki T 1998 Development and characterization of real-time personal neutron dosimeter with two silicon detectors *Nucl. Instrum. Methods Phys. Res.* **418** 465–75
- [52] Andersson Sund E et al 2009 The thin-foil magnetic proton recoil neutron spectrometer MPRu at JET *Nucl. Instrum. Methods Phys. Res. A* **610** 682–99
- [53] Ziegler J 2015 *SRIM and TRIM 2013* (<http://www.srim.org>) (accessed 7 July 2015)
- [54] Ruby L 1994 Further comments on the geometrical efficiency of a parallel-disk source and detector system *Nucl. Instrum. Methods Phys. Res. A* **337** 531–3
- [55] Chichester D L and Seabury E H 2009 Active neutron interrogation to detect shielded fissionable material *Proc. Int. Topical Meeting on Nuclear Research Applications and Utilization of Accelerators* (Vienna: International Atomic Energy Agency)
- [56] BS ISO 8529-1 2001 *Reference Neutron Radiations. Characteristics and Methods of Production* (International Organization for Standardization)
- [57] Souw E-K and Meilunas R J 1997 Response of CVD diamond detectors to alpha radiation *Nucl. Instrum. Methods Phys. Res. A* **400** 69–86
- [58] Malm H L and Martini M 1974 Polarization phenomena in CdTe nuclear radiation detectors *IEEE Trans. Nucl. Sci.* **21** 322–30
- [59] Mersi S, Borchi E, Bruzzi M, D'Alessandro R, Lagomarsino S and Sciortino S 2004 A study of charge collection processes on polycrystalline diamond detectors *Nucl. Instrum. Methods Phys. Res. A* **530** 146–51
- [60] Ivanov A M, Stokan N B and Lebedev A A 2012 Radiation resistance of wide-gap materials as exemplified by SiC nuclear radiation detectors *Tech. Phys.* **57** 556–60
- [61] Bell R, Entine G and Serreze H B 1974 Time-dependent polarization of CdTe gamma-ray detectors *Nucl. Instrum. Methods* **117** 267–71
- [62] Giacomelli L et al 2011 Diamond detectors for fast neutron irradiation experiments *Nucl. Phys. B* **215** 242–6
- [63] Muraro A et al and JET Contributors 2016 First neutron spectroscopy measurements with a pixelated diamond detector at JET *Rev. Sci. Instrum.* **87** 11D833
- [64] Buden R L and Faires J D 1993 *Numerical Analysis* (Boston: PWS)